Organization of Neural Population Code in Mouse Visual System

Kathleen Esfahany*[1, 3], Isabel Siergiej*[2, 3, 4], Yuan Zhao[3], and Il Memming Park[3, 4]

[1]Ward Melville High School, East Setauket, NY, USA
[2]Department of Computer Science, Cornell University, Ithaca, NY, USA
[3]Department of Neurobiology and Behavior, Stony Brook University, Stony Brook, NY, USA
[4]Institute for Advanced Computational Science, Stony Brook University, Stony Brook, NY, USA

Abstract

The mammalian visual system consists of several anatomically distinct areas, layers, and cell types. To understand the role of these subpopulations in visual information processing, we analyzed neural signals recorded from excitatory neurons from various anatomical and functional structures. For each of 186 mice, one of six genetically tagged cell-types and one of six visual areas were targeted while the mouse was passively viewing various visual stimuli. We trained linear classifiers to decode one of six visual stimulus categories with distinct spatiotemporal structures from the population neural activity. We found that neurons in both the primary visual cortex and secondary visual areas show varying degrees of stimulus-specific decodability, and neurons in superficial layers tend to be more informative about the stimulus categories. Additional decoding analyses of directional motion were consistent with these findings. We observed synergy and redundancy in the population code of direction in several visual areas suggesting area-specific organization of information representation across neurons. These differences in decoding capacities shed light on the specialized organization of neural information processing across anatomically distinct subpopulations, and further establish the mouse as a model for understanding visual perception.

Introduction

Though the mouse has long been neglected as a model for studying neural visual information processing, it has recently emerged as a powerful alternative to primate and other carnivorous species. Mice offer the benefit of large-scale, high-throughput experiments and sophisticated genetic tools for investigating highly specific components of visual perception Arenkiel and Ehlers (2009). However, the use of mice in studying visual perception is currently limited by insufficient knowledge about the functional organization of the mouse visual cortex. Thus, we aim to characterize the population neural code associated with cortical organization of visual information processing.

Visual information is thought to be processed in a series of computations as it travels from the retina to the lateral geniculate nucleus and then through a series of visual cortices Nassi and Callaway (2009). The early visual system processes complex visual stimuli through the simultaneous encoding of different stimulus attributes, such as direction, orientation, and spatial and temporal frequency by individual neurons, while higher order visual cortices process nonlinear features Orban (2008). If we can build a simple population decoder to read out the information made accessible

by the neural population (Fig. 1), we can provide insight to which of these features are encoded in specific populations of neurons Graf et al. (2011).

The global topographic organization of the mouse visual cortex has been well characterized. Recent studies have retinotopically identified at least ten visual areas with organized and complete representations of the entire visual field Garrett et al. (2014), Marshel et al. (2011), Wang and Burkhalter (2007). However, the neural population code — how information is collectively represented in the neural activity — has remained elusive. While progress has been made in identifying differences between the spatiotemporal information encoded by neurons in different visual areas, prior work has focused on single neurons and lacks analysis at the population level Andermann et al. (2011), Marshel et al. (2011). By decoding neural responses in large neural populations of 186 mice spanning six visual areas, we aim to better understand population coding in the mouse visual cortex.

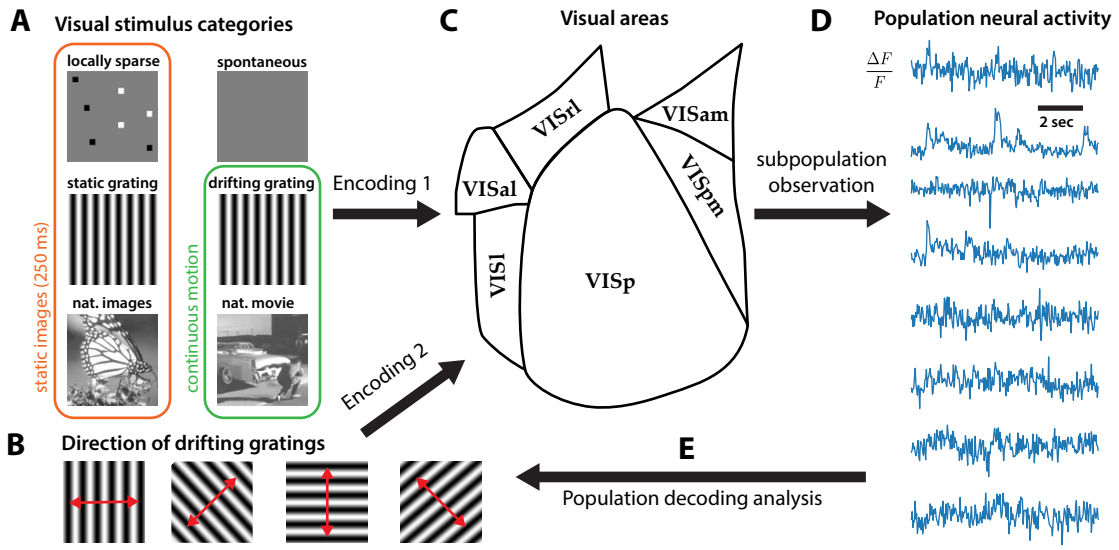

Figure 1: Overview of the population decoding analysis. The neural code of either one of six visual categories (**A**) or one out of eight directions of drifting grating stimulus (**B**) by the excitatory neurons in the mouse visual system (**C**) were analyzed. A specific subpopulation (visual area, cell-type, depth) were targeted and observed while the mice viewed the visual stimuli. From the normalized fluorescence signals from the subpopulation (**D**), we decoded the identity of the stimulus class (**E**). Successful decoding provides evidence for a instantaneous representation of the spatiotemporal signatures of stimuli within the population activity.

Given neural responses from populations of just over one hundred visual cortical neurons, linear classifiers achieve high accuracy in two decoding tasks: one with six stimulus classes with complex spatiotemporal features and one with eight drifting grating directions. We found differential decoding accuracy between the primary (VISp), lateral (VISl), anterolateral (VISal), anteromedial (VISam), posteromedial (VISpm), and rostrolateral (VISrl) visual areas, which implies differential information representation in these visual areas. We also found differences between populations from different cortical depths, with superficial layer populations containing more information than those from deeper layers. Moreover, we found evidence that directional tuning in individual neurons does not necessarily predict the population decoding accuracy suggesting distributed representation of information. These results reveal novel evidence about the cortical organization of visual

information processing.

Materials & Methods

Dataset

We analyzed data from the Allen Brain Observatory[1], downloaded on July 3, 2017 using the AllenSDK version 0.13.2[2]. A full description of the Allen Brain Observatory's data collection methodology is available in their Visual Coding Overview and Visual Stimuli technical whitepapers Allen Institute for Brain Science (2017). In brief, the Allen Brain Observatory recorded *in vivo* two-photon calcium imaging data at 30 Hz over a 400 µm field of view at a resolution of 512×512 pixels. We use data only from mice for which populations of at least ten common neurons were recorded across three visual stimulus sessions, a criterion met by 187 of the 199 mice imaged by the Allen Brain Observatory. Data from one of these 187 mice was further discarded due to a large number of missing values. The sizes (Table S1- S4) and Cre lines (Table S5 and S6) of the populations varied among the targeted visual areas and depths.

A set of synthetic and natural stimuli, comprised of (1) drifting gratings, (2) static gratings, (3) locally sparse noise, (4) natural images, (5) natural movies, and (6) spontaneous activity (mean luminance gray), were displayed on an ASUS PA248Q LCD monitor at a resolution of 1920×1200 pixels, positioned 15 cm from the right eye of head-fixed mice. Spherical warping was applied to all stimuli to account for the close viewing angle. The stimuli were distributed into three sessions A, B, and C (or C2) which were presented over three days. The natural movie and spontaneous stimuli were presented in all sessions. Drifting gratings were presented in session A, static gratings and natural images in session B, and locally sparse noise in session C/C2. Session types C and C2 both contained the 4-degree locally sparse noise stimulus (16×28 array of $4.65°$ patches). Session C2 also contained the 8-degree locally sparse noise stimulus (8×14 array of $9.3°$ patches), which was discarded from analysis since it was only shown to a subset of mice.

The drifting gratings stimulus was comprised of 40 grating conditions (combinations of one of 8 directions and one of 5 temporal frequencies), presented 15 times each in a random order. Each grating was presented for two seconds, followed by one second of mean luminance gray.

Pre-processing

The neural signal was quantified as fluorescence fluctuation $\Delta F/F$, calculated for each frame as $\Delta F/F = \frac{F-F_0}{F_0}$, where the baseline F_0 is the mean fluorescence of the preceding 1 second. For each of 186 neural populations, three hours of $\Delta F/F$ traces were separated into stimulus epochs.

To form samples for the stimulus classification, each epoch was divided into 10 s intervals, of which the final interval was discarded if it was less than 10 s. Neural populations used in the stimulus classification were composed of neurons common across the three imaging sessions A, B, and C (or C2) for each mouse (Table S1 and S2). For each 10 s interval, the mean fluorescence fluctuation per neuron was calculated and labeled with the corresponding stimulus class.

To form samples for the direction classification, the drifting gratings epoch was divided into 3 s intervals, of which the third second (during which a blank sweep of mean luminance gray was presented) was discarded. Neural populations used in the direction classification were composed of all neurons imaged during session A, and thus were larger than populations used in the stimulus

[1] `http://observatory.brain-map.org/visualcoding/`
[2] `https://github.com/AllenInstitute/AllenSDK/`

classification (Table S3 and S4). For each 2 s interval, the mean fluorescence fluctuation per neuron was calculated and labeled with the corresponding grating direction.

In both the stimulus and the direction decoding, mean $\Delta F/F$ for each neuron were z-scored and combined to form the neural feature vectors in $\mathbb{R}^n$ for classification, where n is the number of neurons in the population.

Neural decoding

We used linear classifiers to decode the stimulus classes based on the neural feature vectors. The classifiers were implemented in the Python programming language using the scikit-learn machine learning library version 0.19.0 Pedregosa et al. (2011). Linear support vector machine (SVM)[3] and multinomial logistic regression (MLR)[4] were trained and tested with a nested cross-validation scheme. We principally split the data into training and test sets to form a 5-fold cross-validated prediction.

All results are based on data from both SVM and MLR classification, for which similar results were obtained (Fig. S1). However, we show only show SVM classification results in Figures 2–6 for simplicity.

Due to the different duration of stimulus presentations, the stimulus classes had unbalanced numbers of samples. To build balanced training sets, we subsampled (without replacement) an equal number of responses from each class. The size of these subsamples was equal to 80% of the smallest class (spontaneous activity; 20 minutes out of total 177 or 156 minutes of recording used in samples, depending on if the mouse was shown C or C2). The test sets consisted of the remaining samples, and were kept unbalanced.

The direction classes used in the direction decoding were evenly distributed throughout the stimulus presentation. The direction samples were randomly split intro training (80%) and test (20%) sets for all classification. The training set was assumed to be balanced due to the even distribution of classes throughout data collection.

Both classifiers were regularized using Additive ℓ_2-regularizer of the form $\frac{1}{2C}\|\theta\|^2$. The regularization constant was optimized through a nested cross-validation within the first training set where the best $C = \{10^{-2}, 10^{-1}, 1, 10, 10^2, 10^3, \infty\}$ that yielded the highest accuracy was chosen.

Subsampled population

To investigate the scaling of decoding performance as a function of population size, we made random subsamples (without replacement) of different sizes $n = \{2^0, 2^1, 2^2, \ldots\}$ up to the number of neurons available for each mouse. We repeated the procedure 10 times to form 10 resampled subpopulations. We report accuracy values averaged over the ten resampled datasets. The statistics of population sizes by group or decoding task can be found in Table S1–S4.

Accuracy curve fitting

To extrapolate the accuracy as a function of population size, we used the following generalized logistic function:

$$\text{accuracy}(n) = \frac{1-c}{(1+e^{-an})^b} + c, \tag{1}$$

[3] `LinearSVC` in `scikit-learn`

[4] `LogisticRegression` with two parameters `multi_class = 'multinomial'` and `solve='lbfgs'` in `scikit-learn`

with 3 parameters $\{a, b, c\}$ with constraints $a \geq 0, c \geq 0$ and $b \in [0, 1]$. Note that the c parameter allows a minimum accuracy expected from chance level performance for small population size. We fit the curve on the average accuracies obtained by subsampling using nonlinear least squares[5] van der Walt et al. (2011).

Statistical tests

To compare accuracy between cortical areas and imaging depths, we performed Tukey's test at a 0.05 significance level Tukey (1949). Tukey's test compares the mean accuracies of every pair with adjustment for multiple comparison. Ten imaging depths (175 µm, 265 µm, 275 µm, 300 µm, 325 µm, 335 µm, 350 µm, 365 µm, 375 µm, 435 µm) were sorted into four groups: 175 µm, 265-300 µm, 325-350 µm, and 365-435 µm. We compared the six visual cortical areas (VISp, VISpm, VISl, VISal, VISam, and VISrl), four imaging depth groups, and six stimulus classes.

Orientation and Direction Selectivity

The neural activity recorded during the Session A drifting gratings stimulus was used to calculate the orientation selectivity index (OSI) and direction selectivity index (DSI) for each neuron. We obtained OSI and DSI using the Allen SDK Drifting Gratings module. The full computation methodology for these indices can be found in the Allen Brain Observatory's Visual Stimuli technical whitepaper. To compare across visual areas, the OSI and DSI of all neurons in each area were averaged together (Fig. 4D,E). To compare across depths, the OSI and DSI of all neurons in each depth were averaged together (Fig. 6D,E).

Results

Spatiotemporal structure of stimuli are differentially encoded among visual areas

To investigate differences in information processing between six mouse visual areas, statistical classifiers were fit to discriminate visual categories based on the population activity within each area. Neural activity was monitored through a fluorescent calcium sensor (GCaMP6) selectively expressed in transgenic mice Allen Institute for Brain Science (2017). Recorded calcium signals were processed and discretized in time to yield feature vectors corresponding to neural activity of the population (see Methods). Mice were shown six types of stimuli which differed in their spatiotemporal structures, ranging from simple spatial structures (such as orientation gratings and sparse pixels) to complex natural scenes. The stimuli included static images as well as movies with complex long range correlations. A faithful recovery of these visual categories from neural activity reflects the potential information the neural population encodes about the stimuli.

Since the population size was variable across experiments, we compare the rate at which the classification accuracy improves as a function of population size (Fig. 2A). Classification accuracies from small randomly subsampled populations were near chance level, and gradually increased with the population size for all sessions analyzed (Fig. 2A; black dots). We fit a 3-parameter sigmoid function to extrapolate up to 128 neurons for each session (Fig. 2A; see Methods). The averages within each of the six visual areas show similar increasing trends with accuracy approaching 90% for the population size of 128. However, five areas (VISal, VISam, VISl, VISp, VISpm) significantly outperformed VISrl (Fig. 2B,C).

[5] `scipy.optimize.curve_fit`

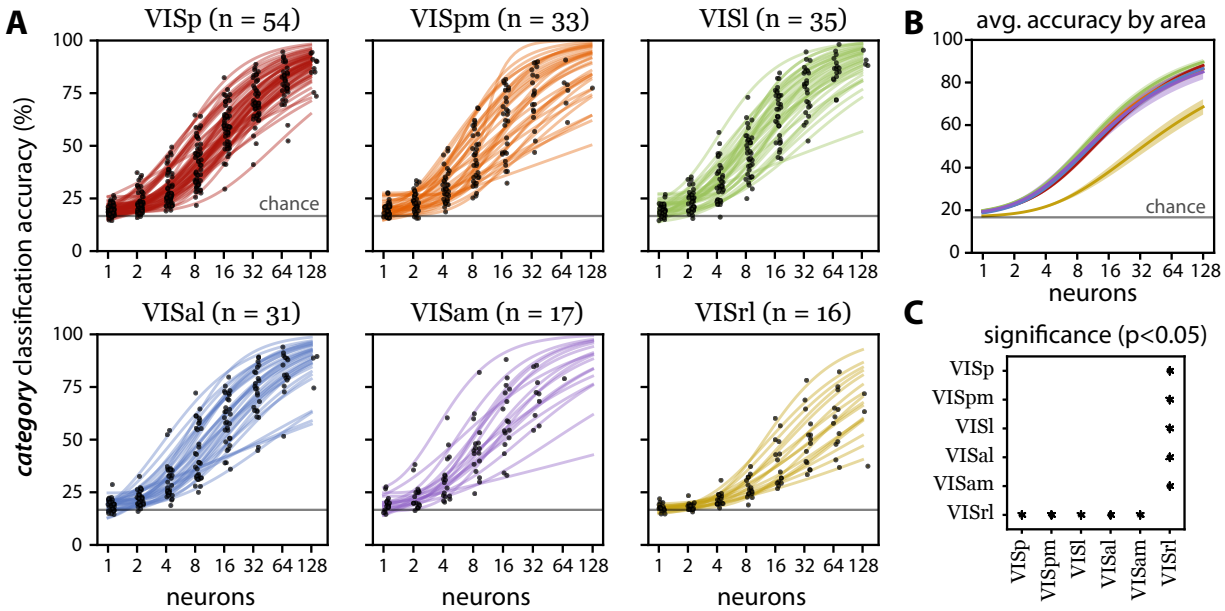

Figure 2: Population decoding performance by visual area for six stimulus classes. (**A**) Stimulus decoding accuracy for individual randomly subsampled populations consisting of 1, 2, 4, 8, 16, 32, 64, and 128 neurons (black dots, jittered for visual clarity) and curve fits (solid lines). The number of populations per area is listed in the titles (n). In all visual areas, the majority of small populations (1-4 neurons) outperformed chance level (gray line at 16.67 % accuracy). However, small population performance in VISrl was more concentrated near chance level than all other areas. Individual populations of 128 neurons achieved near-perfect accuracy in all visual areas except VISrl. (**B**) Population averaged accuracy by visual area (solid lines) with standard error (shaded regions). The line colors correspond to the visual area indicated by the line colors in **A**. (**C**) Statistically significant ($p < 0.05$) pairwise comparisons of decoding accuracy at 128 neurons between the six visual areas using Tukey's test. VISrl underperforms all other visual areas.

To investigate whether such similarity holds for each subcategory, we analyzed accuracy in decoding specific stimuli. Though similar in overall decoding accuracy, these five high-performing visual areas show differential pattern in per category accuracy (Fig. 3). On average, natural movie and spontaneous categories were more difficult to decode (Fig. 3B,C). The natural movie category is significantly harder to decode than other stimuli in populations from the anatomically adjacent VISp, VISl, and VISal (Fig. 3A).

Area dependent decoding of drifting gratings direction

In many animals' primary visual cortex, local visual orientation information is first processed Hubel and Wiesel (1959). Layer 2/3 neurons in the mouse visual cortex are also sensitive to orientation gratings and their directional motion Marshel et al. (2011). However, mouse primary visual cortex seems to also serve the role of higher order visual function Gavornik and Bear (2014). We investigated if the ability to decode vastly different stimulus categories is related to their capacity to represent orientation and direction. Using the average neural activity in 2-second windows corresponding to the duration of drifting grating presentation, we trained linear classifiers to decode the direction of drifting gratings.

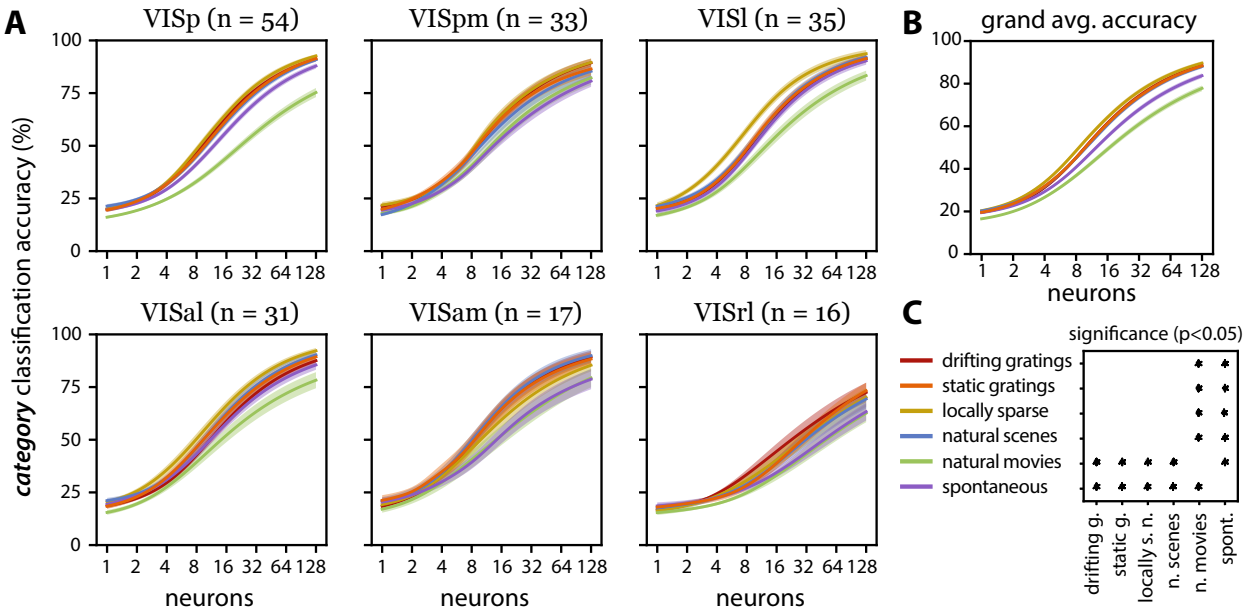

Figure 3: Stimulus-specific population decoding. (**A**) Visual area averaged stimulus-specific decoding accuracy similar to Fig. 2. The line color corresponds to the stimulus indicated by the legend in **C**. High-performing areas with similar overall decoding accuracy show differential accuracy in predicting specific stimuli. (**B**) Stimulus-specific decoding accuracy averaged across all populations. There is differential accuracy in decoding the specific stimulus classes, with some being harder to decode than others. (**C**) Statistical significance map (same convention as Fig. 2C). The natural movies are significantly more difficult to decode than all other stimuli, and the locally sparse noise is significantly more difficult to decode than all others except the natural movies.

Except for a few VISrl recording sessions, direction decoding was again an increasing function of population size (Fig. 4A). VISrl showed the worst decoding performance at the 128 neuron level, and VISam/VISpm showed intermediate performance, but VISp, VISl and VISal showed comparable population level encoding (Fig. 4B,C).

Surprisingly, the population decoding accuracy showed discrepancies from what is expected from individual neuron's directional tuning sensitivity. Higher orientation and direction selectivity index (Fig. 4D,E) indicates the stronger representation of these basic visual features, which is highest in VISl followed by VISrl. However, the joint activity decoding showed VISl being on par with VISp and VISal, while the VISrl population was less informative. This suggests that excitatory neurons in VISp and VISal are more synergistic (a tendency for the population to contain more information than individual neurons Brenner et al. (2017), Latham and Nirenberg (2005)) and there is relatively more redundancy in the VISrl population.

Superficial layers are more informative about the spatiotemporal signatures of visual stimuli

In rats, neurons in the superficial layers of V1 are known to have better orientation selectivity and less spontaneous activity Girman et al. (1999), suggesting a laminar organization of visual information processing. To investigate if similar laminar differences exists in mice, we analyzed the decoding accuracy of stimulus classes as a function of recording depth (Fig. 5). Excitatory

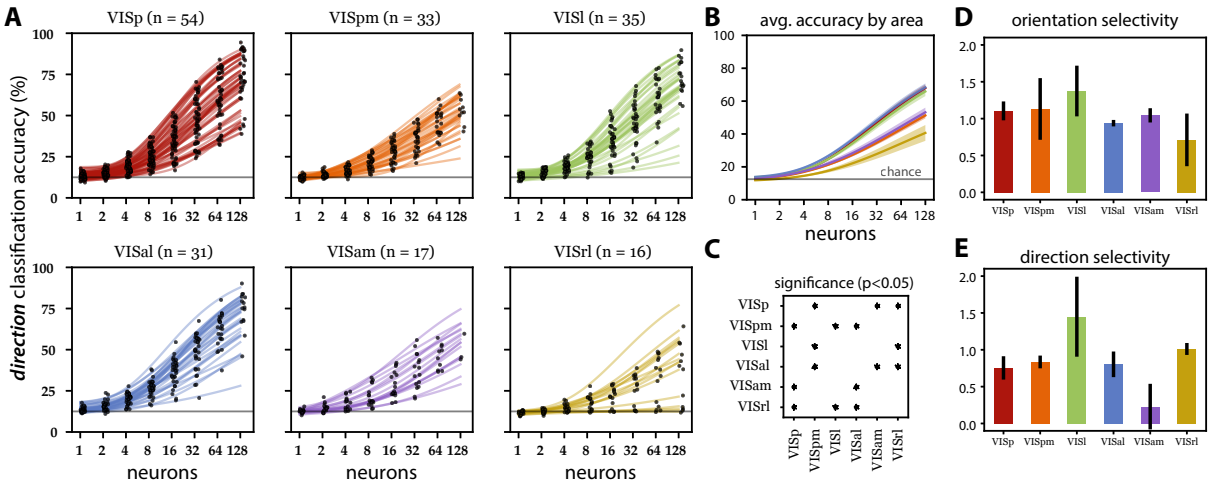

Figure 4: Population decoding of directions for the drifting grating epoch. (**A**) Direction decoding accuracy (same conventions as Fig. 2). Note that in VISrl, small populations (1-2 neurons) performed closer to chance level (gray line at 12.5 % accuracy) than the same sized populations in other areas. (**B**) Population averaged accuracy by visual area (solid lines) with standard error (shaded regions). The line colors correspond to the visual area indicated by the line colors in **A**. (**C**) Statistical significance map (same convention as Fig. 2C). Three high-performing, areas (VISp, VISal, VISl) showing similar performance are anatomically adjacent. Similarly, two of three low-performing areas (VISpm and VISam) showing similar performance are anatomically adjacent. (**D,E**) Mean orientation (D) and direction (E) selectivity index (with SEM) per area (see Methods).

neurons in the superficial layers (corresponding to imaging depths of 175 µm, putative layer 2/3) significantly outperformed the deeper populations (Fig. 5). There were 6 different Cre lines with specific targets; superficial layer corresponded to either Cux2 or Emx1 Cre lines (see Table S6 for full distribution). There were little difference across Cre lines, hence we present the results grouped by depth. The 325–350 µm depth group (either Nr5a1 or Scnn1a Cre lines) showed worst visual category decoding performance, consistent with the direction decoding task results (Fig. 6). However, the superficial layer did not show distinctly superior direction decoding (Fig. 6B). This suggests that the spatiotemporal structure of each visual category extra to the overall orientation information is better represented in the superficial layers.

The orientation selectivity index (OSI) and DSI showed contrary trends (Fig. 6D,E). Deeper layers had relatively larger OSI but smaller DSI, indicating the temporal component of the drifting gratings is better represented in the superficial layer. Despite larger DSI, the 325–350 µm group performed worse than the 365–435 µm group, again an unexpected observation likely due to the spatial organization of the code.

Discussion

The focus of this study was investigating how stimulus classes and drifting grating directions can be inferred from neural population responses in mouse visual areas. In primates, it has been well established that visual processing occurs through a hierarchical structure, in which the primary visual cortex provides input to secondary visual areas Felleman and Van Essen (1991), Maunsell and Newsome (1987), Orban (2008). The rat visual cortex has also been characterized as having

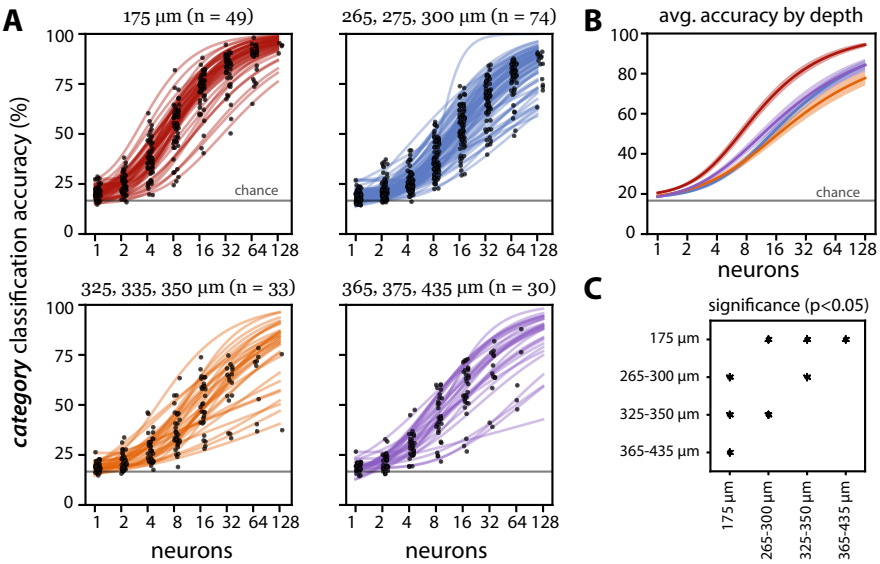

Figure 5: Population decoding performance by recording depth for six stimulus classes. (same conventions as Fig. 2). On average, small populations (1-2 neurons) performed better than chance level performance (gray line at 16.67% accuracy). The 325–350 µm group significantly underperforms two shallower groups (175 µm and 265–300 µm).

a hierarchical organization Coogan and Burkhalter (1993). Results from this analysis corroborate recent studies which have suggested that this simple hierarchy may also be present in the mouse visual cortex Berezovskii et al. (2011), Wang and Burkhalter (2007). In both decoding tasks, the overall decoding performance of populations from secondary visual areas was equal to or worse than the primary visual cortex (VISp), suggesting that secondary areas do not encode any more information than is encoded by the primary visual cortex. This is supported by findings that the mouse primary visual cortex has a more diverse set of stimulus preferences than secondary areas VISal and VISpm Andermann et al. (2011).

Differences in stimulus-specific decoding performance between populations from different visual areas suggest areal differences in visual information representation. On average, the spontaneous stimulus and the natural move stimulus are significantly harder to decode than other stimuli, but this trend is not seen in all areas (Fig 3). Anatomically adjacent visual areas display similarities in their stimulus-specific decoding performance. The adjacent anteromedial (VISam) and posteromedial (VISpm) areas showed no difference in performance for specific stimuli. In contrast, in populations from the adjacent primary (VISp), anterolateral (VISal), and lateral (VISl) visual areas, it was significantly harder to decode the natural movie stimulus than other stimuli. These anatomical trends in stimulus-specific decoding may be attributed to specialized input pathways from the primary visual cortex Marshel et al. (2011).

The existence of these information processing streams is further supported by the similar direction decoding performance of anatomically adjacent areas. The same groups emerge in the direction decoding as in the stimulus-specific analysis. The adjacent primary (VISp), anterolateral (VISal) and lateral (VISl) visual areas performed similarly, as did the adjacent antermedial (VISam) and posteromedial (VISpm) areas. The poor performance of the latter group of visual areas (VISam and VISpm) as well as the rostrolateral (VISrl) visual area suggests a lack of direction sensitive information encoding.

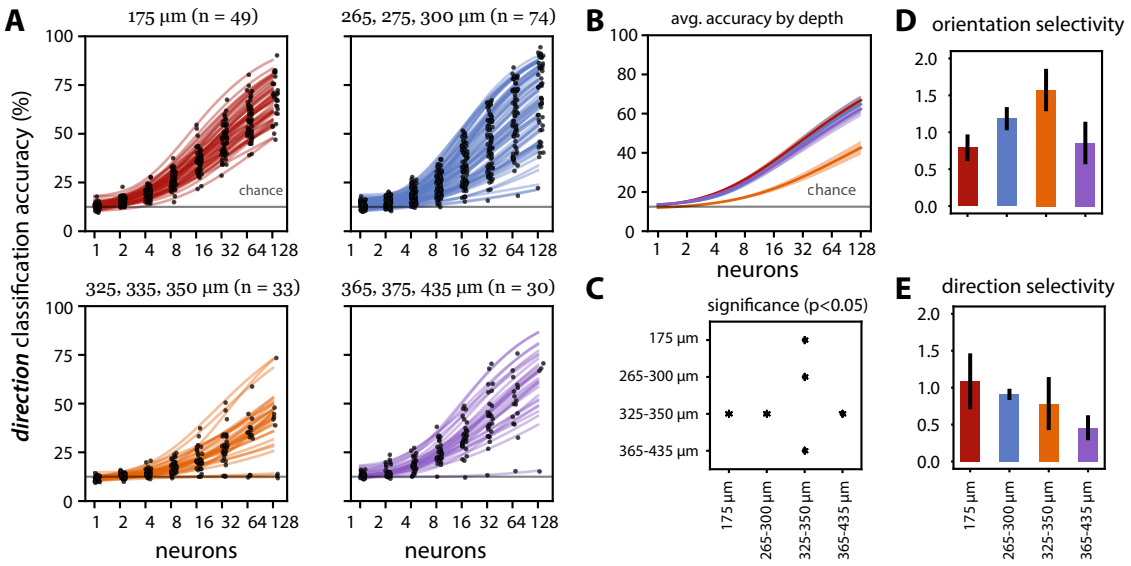

Figure 6: Population decoding performance by imaging depth for eight drifting grating directions. (same conventions as Fig. 4). On average, small populations (1-2 neurons) in the three high performing depth groups (175 µm, 265–300 µm, and 365–435 µm) outperformed chance level (gray line at 12.5% accuracy), while small populations in the low-performing 325–350 µm group performed at chance level.

Marshel et al. (2011) presented drifting bar and drifting grating stimuli to 28 mice and found, based on the mean direction selectivity index (DSI) of each area and the proportion of neurons with a DSI greater than 0.5, that layer 2/3 (130-180 µm below the dura surface) populations in the anterolateral (VISal), rostrolateral (VISrl), and anteromedial (VISam) visual areas were significantly more direction selective than the primary visual cortex (VISp). The results of our population direction decoding analysis of 186 mice are inconsistent with the single neuron findings of Marshel et al. (2011) (note that there were differences in the methods for estimating DSI; see Methods). The direction decoding accuracy of VISam and VISrl populations are significantly lower than that of VISp, suggesting that these populations are less direction selective than those in VISp. Spatial organization of information or spatial correlations could contribute to such discrepancies Averbeck et al. (2006), Brenner et al. (2017). Furthermore, the similar decoding accuracy of VISal and VISp populations suggests that VISal is not significantly different from VISp in its direction selectivity.

Across all visual areas, individual neurons encode enough attributes of a stimulus in their responses that the majority of small populations outperformed chance level accuracy in the stimulus decoding (chance equal to 16.67 %) as well as in the direction decoding (chance equal to 12.5 %). However, in the direction decoding, individual neurons from VISrl populations and those from the 325–350 µm depth group performed at chance level, suggesting a lower proportion of direction sensitive encoding in these neurons relative to other areas and depths. Neurons in VISam have previously been characterized as extremely robust and selective Marshel et al. (2011). However, our direction decoding analysis shows that decoding accuracy for small VISam populations of 1-4 neurons remains at or close to chance level, suggesting that these neurons are not especially selective. Even with larger VISam populations, direction decoding accuracy remained low relative to other areas.

Despite some discrepancies with recent characterizations of mouse visual areas, this study pro-

vides novel evidence of the functional and anatomical organization of the mouse visual cortex. The results corroborate broad trends in visual information processing, supporting the existence of a hierarchical organization and information processing streams in the mouse visual cortex.

Acknowledgement

We would like to thank Michael Buice for thoughtful discussions. We would also like to thank the Allen Institute for Brain Science for supporting open data and open science. This work was partially supported by the Simons Summer Research Program hosted by Stony Brook University.

References

Allen Institute for Brain Science (2017). Visual coding overview. `http://observatory.brain-map.org/visualcoding/`. accessed: 2017 July 1.

Andermann, M. L., Kerlin, A. M., Roumis, D. K., Glickfeld, L. L., and Reid, R. C. (2011). Functional specialization of mouse higher visual cortical areas. *Neuron*, 72(6):1025–1039.

Arenkiel, B. R. and Ehlers, M. D. (2009). Molecular genetics and imaging technologies for circuit-based neuroanatomy. *Nature*, 461(7266):900–907.

Averbeck, B. B., Latham, P. E., and Pouget, A. (2006). Neural correlations, population coding and computation. *Nature Reviews Neuroscience*, 7(5):358–366.

Berezovskii, V. K., Nassi, J. J., and Born, R. T. (2011). Segregation of feedforward and feedback projections in mouse visual cortex. *The Journal of Comparative Neurology*, 519(18):3672–3683.

Brenner, N., Bialek, W., and de Ruyter van Steveninck, R. (2017). Adaptive rescaling maximizes information transmission. *Neuron*, 26(3):695–702.

Coogan, T. A. and Burkhalter, A. (1993). Hierarchical organization of areas in rat visual cortex. *The Journal of neuroscience : the official journal of the Society for Neuroscience*, 13(9):3749–72.

Felleman, D. J. and Van Essen, D. C. (1991). Distributed hierarchical processing in the primate cerebral cortex. *Cerebral cortex (New York, N.Y. : 1991)*, 1(1):1–47.

Garrett, M. E., Nauhaus, I., Marshel, J. H., and Callaway, E. M. (2014). Topography and areal organization of mouse visual cortex. *Journal of Neuroscience*, 34(37):12587–12600.

Gavornik, J. P. and Bear, M. F. (2014). Learned spatiotemporal sequence recognition and prediction in primary visual cortex. *Nature Neuroscience*, 17(5):732–737.

Girman, S. V., Sauvé, Y., and Lund, R. D. (1999). Receptive field properties of single neurons in rat primary visual cortex. *Journal of Neurophysiology*, 82(1):301–311.

Graf, A. B. A., Kohn, A., Jazayeri, M., and Movshon, J. A. (2011). Decoding the activity of neuronal populations in macaque primary visual cortex. *Nature Neuroscience*, 14(2):239–245.

Hubel, D. H. and Wiesel, T. N. (1959). Receptive fields of single neurones in the cat's striate cortex. *The Journal of physiology*, 148:574–591.

Latham, P. and Nirenberg, S. (2005). Synergy, redundancy, and independence in population codes, revisited. *J. Neurosci.*, 25(21):5195–5206.

Marshel, J. H., Garrett, M. E., Nauhaus, I., and Callaway, E. M. (2011). Functional specialization of seven mouse visual cortical areas. *Neuron*, 72(6):1040–1054.

Maunsell, J. H. R. and Newsome, W. T. (1987). Visual processing in monkey extrastriate cortex. *Annual Review of Neuroscience*, 10(1):363–401.

Nassi, J. J. and Callaway, E. M. (2009). Parallel processing strategies of the primate visual system. *Nature Reviews Neuroscience*, 10(5):360–372.

Orban, G. A. (2008). Higher order visual processing in macaque extrastriate cortex. *Physiological Reviews*, 88(1):59–89.

Pedregosa, F., Varoquaux, G., Gramfort, A., Michel, V., Thirion, B., Grisel, O., Blondel, M., Prettenhofer, P., Weiss, R., Dubourg, V., Vanderplas, J., Passos, A., Cournapeau, D., Brucher, M., Perrot, M., and Duchesnay, E. (2011). Scikit-learn: Machine learning in Python. *Journal of Machine Learning Research*, 12:2825–2830.

Tukey, J. W. (1949). Comparing individual means in the analysis of variance. *Biometrics*, 5(2):99–114.

van der Walt, S., Colbert, S. C., and Varoquaux, G. (2011). The NumPy array: A structure for efficient numerical computation. *Computing in Science & Engineering*, 13(2):22–30.

Wang, Q. and Burkhalter, A. (2007). Area map of mouse visual cortex. *The Journal of Comparative Neurology*, 502(3):339–357.

Supplementary material

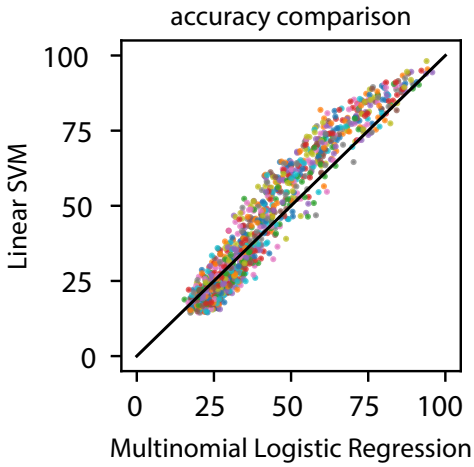

Figure S1: Comparison of results of linear support vector machine (SVM) and multinomial logistic regression (MLR) classification. SVM and MLR classification accuracy for subsampled populations of 1, 2, 4, 8, 16, 32, 64, and 128 neurons are represented by a single point. Similar results were achieved by both classifiers.

Table S1: Mean population size with standard deviation by visual area for the stimulus classification. Populations are composed of neurons common across the three imaging sessions A, B, and C.

Area	VISal	VISam	VISl	VISp	VISpm	VISrl
Mean Pop. Size	65.16	38.12	69.71	82.91	42.42	92.00
Std. Deviation	40.89	18.53	43.45	48.96	27.08	37.64

Table S2: Mean population size with standard deviation by imaging depth group for the stimulus classification. Populations are composed of neurons common across the three imaging sessions A, B, and C.

Imaging Depth (µm)	175	265-300	325-350	365-435
Mean Pop. Size	70.82	84.96	46.82	38.50
Std. Deviation	33.74	50.14	34.20	22.62

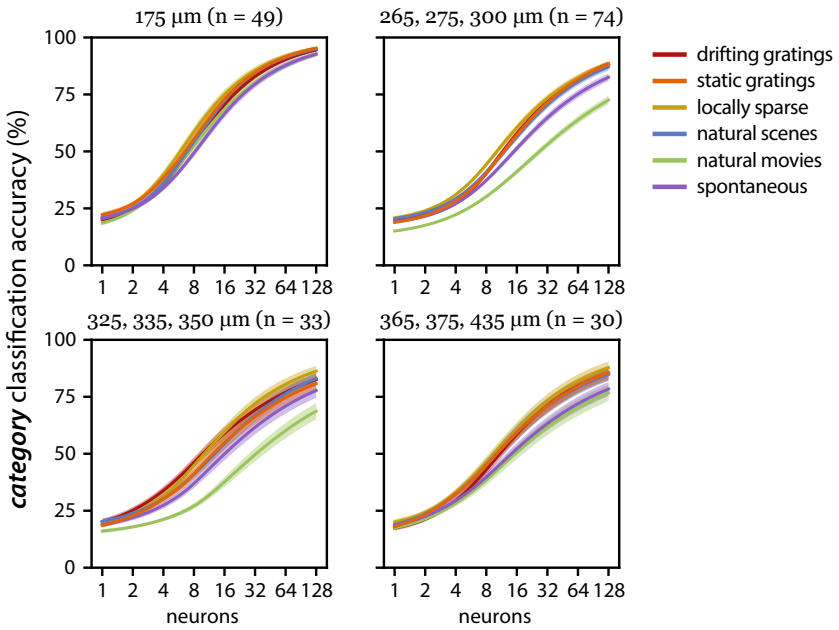

Figure S2: Stimulus-specific decoding performance by imaging depth group. The highest performing depth (175 µm) and a lower performing group (365-435 µm) show uniform accuracy in decoding all six stimuli. In the 265-300 µm and 325-350 µm groups, natural movies are significantly harder to decode than other stimuli.

Table S3: Mean population size with standard deviation by visual area for the direction classification. Population sizes are larger for the direction classification than the stimulus classification because the population includes all neurons imaged in Session A.

Area	VISal	VISam	VISl	VISp	VISpm	VISrl
Mean Pop. Size	139.13	89.12	143.97	169.87	99.87	178.13
Std. Deviation	79.40	56.77	85.16	84.83	62.29	68.83

Table S4: Mean population size with standard deviation by imaging depth group for the direction classification. Population sizes are larger for the direction classification than the stimulus classification because the population includes all neurons imaged in Session A.

Imaging Depth (µm)	175	265-300	325-350	365-435
Mean Pop. Size	153.49	178.15	93.27	80.13
Std. Deviation	56.76	88.79	66.22	52.75

Table S5: Cre line populations in each visual area.

Area	VISal	VISam	VISl	VISp	VISpm	VISrl
Cux2-CreERT2	11	5	13	16	13	3
Emx1-IRES-Cre	7	2	6	7	4	6
Nr5a1-Cre	4	1	5	9	6	4
Rbp4-Cre_KL100	3	4	5	5	5	1
Rorb-IRES2-Cre	6	5	6	8	5	2
Scnn1a-Tg3-Cre	0	2	0	9	0	0

Table S6: Cre line populations in each depth group.

Imaging Depth (µm)	175	265-300	325-350	365-435
Cux2-CreERT2	34	27	0	0
Emx1-IRES-Cre	15	10	0	7
Nr5a1-Cre	0	3	26	0
Rbp4-Cre_KL100	0	0	0	23
Rorb-IRES2-Cre	0	32	0	0
Scnn1a-Tg3-Cre	0	2	7	0